Foam-embedded Soft Robotic Joint with Inverse Kinematic Modeling by Iterative Self-improving Learning

Anlun Huang, Yongxi Cao, Jiajie Guo, Zhonggui Fang, Yinyin Su, Sicong Liu*, *Member, IEEE,* Juan Yi, *Member, IEEE,* Jian S. Dai, *Fellow, IEEE,* and Zheng Wang*, *Senior Member, IEEE.*

***Abstract*—Soft robotic arms suffer from instability due to their high-elasticity structure, which further leads to the difficulty of precise kinematic modeling. This work introduces a novel solution employing memory foam-embedded joint design (Fe-Joint), effectively mitigating oscillations and enhancing motion stability. This innovation is seamlessly integrated into the new continuum soft robotic arm (Fe-Arm). Through iterative design optimization, Fe-Arm attains superior mechanical performance and control capabilities, enabling a settling state in 0.4 seconds post external force. We propose a long short-term memory network (LSTM) based iterative self-improving learning strategy (ISL) for end-to-end inverse kinematics modeling, tailored to Fe-Arm's mechanical traits, enhancing modeling performance with limited data. Investigating key control parameters, we achieve target trajectory modeling errors within 10% of the workspace radius. Open-loop trajectory tracking substantiates practical model viability and efficiency.**

***Index Terms*—Soft robotic joint, oscillation reduction, self-improving learning.**

I. Introduction

SOFT robotic arms have emerged as a prominent research area within the field of soft robotics, driven by their inherent characteristics of safety, lightweight construction, and compliance [1], [2]. These attributes position them as promising solutions for applications in diverse unstructured environments. Recent studies have reported diverse actuation designs, including pneumatic systems [3], cable-driven mechanisms [4], and electroactive polymers [5]. Notably, continuum soft robotic arm structures typically feature three soft actuators connected in parallel, forming a triangular configuration in cross-section [6], [7]. These innovative designs allow soft robotic arms to exhibit distinctive morphologies that deviate significantly from traditional rigid-body counterparts, opening up possibilities for novel tasks and enhanced functionalities.

Soft robotic arms employing these actuation methods and structure designs have demonstrated promising motion performance when coupled with carefully designed position or dynamics controllers. However, they often face challenges stemming from undesired oscillations in dynamic scenarios. For instance, experimental results from the FESTO Bionic Handling Assistant (BHA) indicate that when subjected to external forces, the robotic arm undergoes under-damped oscillations lasting approximately three seconds before reaching a stable state [8]. Similarly, the multi-segment manipulator powered by fluidic elastomer actuators also experiences an oscillation period of roughly 10 seconds [3]. This phenomenon significantly limits the potential applications of soft robotic arms. The drawbacks associated with undesired oscillation encompass various aspects, including (a) the inability to sustain substantial external loads, (b) diminished image perception when cameras are integrated as part of the end-effector, and (c) the impracticality of implementing high-frequency feedback dynamic controllers. This problem is not due to immature fabrication or poor controller design, but a result of the high inherent compliance of the actuator material. Soft robotic arms, typically composed of stacked soft actuators or joints, possess high elasticity, exacerbating the amplification of oscillations within the system.

The inherent instability of soft robotic arms has driven extensive research into enhancing their mechanical properties. There have been various efforts devoted to increasing the stiffness and load capacity of soft robotic arms, including integrating shape memory alloy [9], particle jamming [10], and antagonistic mechanisms [11]. However, these proposed methods are not fundamentally effective in eliminating the effects of oscillations in soft robotic arms.

Foams have emerged as a novel material in soft robot fabrication, offering diverse benefits. Poroelastic foam has been utilized for the simple fabrication of soft robots [12]. Additionally, polyethylene foam has enabled the construction of human-scale soft robots [13]. Researchers have successfully employed polyurethane foam in the creation of soft grippers and even soft robotic "puppies" [14]. In the context

This work was partly supported by the National Key R&D Program of China (Grant No. 2022YFB4701200), Shenzhen Science and Technology Program Grant JCYJ20220530114615034 and JCYJ20220818100417038, Guangdong Basic and Applied Basic Research Foundation Grant 2021A1515110658 in part by the Guangdong Provincial Key Laboratory of Human-Augmentation and Rehabilitation Robotics in Universities. *(Anlun Huang, Yongxi Cao, and Jiajie Guo are co-first authors.) (Corresponding authors: Sicong Liu and Zheng Wang.)*

Anlun Huang, Yongxi Cao, Jiajie Guo, Zhonggui Fang, Yinyin Su, Sicong Liu, Juan Yi, and Zheng Wang are with the Guangdong Provincial Key Laboratory of Human Augmentation and Rehabilitation Robotics in Universities, Department of Mechanical and Energy Engineering, Southern University of Science and Technology, Shenzhen 518000, China (e-mail: 11912702@mail.sustech.edu.cn; 11811401@mail.sustech.edu.cn; 11811503@mail.sustech.edu.cn; 12231129@mail.sustech.edu.cn; yinyinsu1991@gmail.com; liusc@sustech.edu.cn; yij3@sustech.edu.cn; wangz@sustech.edu.cn).

Jian S. Dai is with the Department of Mechanical and Energy Engineering, Southern University of Science and Technology, Shenzhen 518000, China (e-mail: daijs@sustech.edu.cn). Yinyin Su is also with the Department of Mechanical Engineering, The University of Hong Kong, Hong Kong SAR, China.

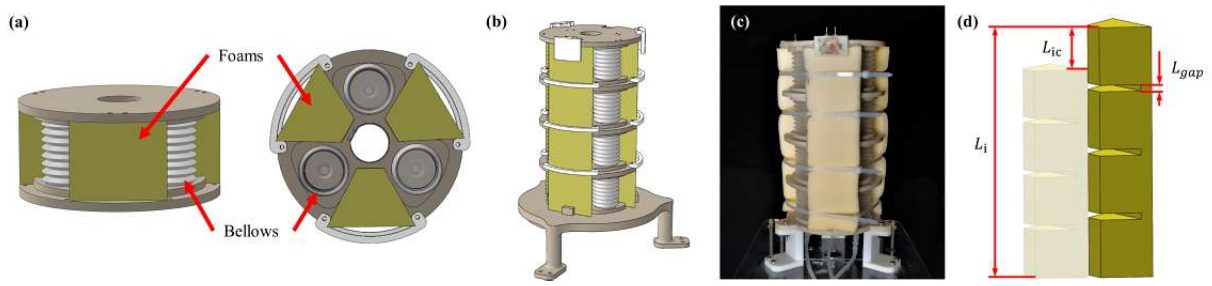

Fig. 1. (a) The Fe-Joint design. (b) The Fe-Arm design. (c) The prototype of Fe-Arm. (d) Embedded foam design and geometrical parameters. L_{gap} is the length of the gap between levels. L_{ic} is the length of the initial compression. L_i is the initial length of the foam.

of pneumatic actuators, polyurethane foam material has also been integrated within vacuum-powered design, achieving a lightweight structure with variable density and high deformation tolerance [15]. Memory foam, a specific type of polyurethane foam, possesses viscoelastic properties and low-resilience characteristics [16], [17], making it highly suitable for structural support and oscillations reduction of soft robotic arms.

In the domain of inverse kinematic modeling for soft robotic joints and arms, due to fabrication errors and the complex dynamics inherent in soft systems, traditional analytical models face challenges in accurately mapping sensor readings to system states. For instance, the widely used Piecewise Constant-curvature method encounters difficulties in this regard [18]. To address these challenges, recent studies in soft robots have explored the application of various machine learning techniques, with a particular focus on deep learning methodologies [19], [20]. Neural networks, such as feed-forward networks (FNNs) and recurrent neural networks (RNNs), have been employed to learn the forward and inverse kinematics of soft continuum joints and planar finger robotic arms [21]. Long short-term memory network (LSTM), a prominent architecture within RNNs, has been trained to explore the best mapping between the sensor data and the 3D shape of pneumatic soft robots [22]. Furthermore, LSTM and gated recurrent unit (GRU) models have been employed to generate kinematic models for proprioceptive redundant receptor systems in soft robots [23].

In the realm of employing deep learning techniques for modeling soft robotic arms, a substantial challenge revolves around acquiring an adequate volume of high-quality labeled training data. Given the scarcity or expense associated with obtaining labeled data, the utilization of self-supervised learning and semi-supervised learning has gained traction in learning paradigms. Notably, while self-supervised learning strategies have been successfully applied to enhance the efficacy of mobile robot navigation [24] and augment the triumph rate of robotic arm grasping [25], their application in soft robots modeling has largely remained unexplored. Self-training, a semi-supervised learning approach, exploits the model's own predictions to generate pseudo-labels for data that is either unlabeled or possesses weak labeling. This technique finds significant utility in domains such as object detection [26] and image classification [27]. The notion of recursively generating high-quality data holds substantial promise in soft robotic learning-based data-driven modeling.

In this paper, we present solutions to address the oscillation problem in soft robotic arms through the design of joints and the challenges in modeling and control. Our proposed approach involves a foam-embedded soft robotic joint, which mitigates undesired oscillations. This joint design is seamlessly integrated into a new continuum soft robotic arm, resulting in improved mechanical motion performance while maintaining inherent compliance and flexibility. To achieve cost-effective control, we employ an LSTM-based iterative self-improving learning method for modeling the arm. We demonstrate the effectiveness of this approach through real motion control experiments. The contributions of this work can be summarized as follows:

- Introduced a novel foam-embedded soft robotic joint design (Fe-Joint) that effectively reduces undesired oscillations in soft robot motion.
- Integrated the Fe-Joint into the new continuum soft robotic arm (Fe-Arm), and defined four key performance metrics to optimize the design further. Realized pneumatic-based active motion control of the Fe-Arm in three degrees of freedom (DOFs).
- Proposed an iterative self-improving learning strategy (ISL) with the LSTM architecture for end-to-end inverse kinematic modeling of the Fe-Arm. Investigated the effect of two control parameters (delay time and step size) on the modeling approach. Achieved a modeling error of less than 10% relative to the maximum horizontal radius of motion, even with limited data availability and human intervention. Successfully executed specific target trajectories under open-loop control.

II. Design and Optimization

A. Foam-embedded Design and Fabrication

As shown in Fig. 1(a), the Fe-Joint is developed by combining distinct dynamic properties of foam and bellows. The active actuation component leverages the high scalability of pneumatic bellows. Blow-molded pneumatic bellows with open ends are employed, concatenating together with 3D-printed nylon planes. To ensure airtightness, we seal the bellows using the hot-melt adhesive (HMA). The passive energy absorption component capitalizes on the viscoelasticity and low resilience of the foam. Each foam is cropped to fit within the space between the bellows, serving as the core

TABLE I
GEOMETRICAL CONFIGURATIONS OF THE FE-ARM

Parameter	Value(unit)
The initial height	240mm
The maximum extension length	255mm
The minimum contraction length	115mm
The maximum radius of cross-section	70mm
The horizontal distance between the two bellows' axis	69.28mm
The maximum diameter of the bellows	37.56mm
The minimum diameter of the bellows	30.94mm

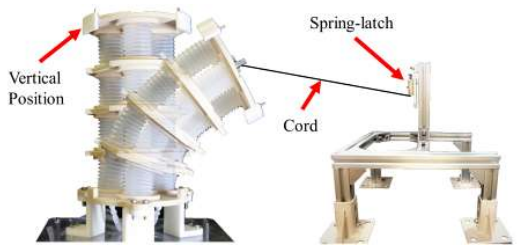

Fig. 2. Schematic diagram of passive evaluation experiment.

element of absorbing elastic potential generated by the bellows during motion.

As illustrated in Fig. 1(b)(c), the Fe-Arm is constructed by connecting four Fe-Joints in series. To reduce the overall system's DOF and mitigate buckling, 3D-printed connectors are used to link each joint and constraint. All bellows actuators in one vertical line are connected internally and share the same pneumatic pressure. This design enables the Fe-Arm to actuate with three independent pressure inputs, resulting in three actuated DOFs. To facilitate the insertion of foam into the Fe-Arm, the foams are cut into specific shapes, as depicted in Fig. 1(d). Additionally, nylon belts are employed to secure the assembled parallel structure at each joint, ensuring the desired curvature shape during movements. Geometrical configurations of the Fe-Arm are shown in TABLE I.

B. Performance Evaluation

To conduct a comparative analysis of different foam-embedded designs and assess their performance, a passive evaluation experiment is employed. Since all Fe-Joints within the Fe-Arm exhibit the same mechanical characteristics, the Fe-Arm itself is used for performance testing, as it can effectively amplify the results. As shown in Fig. 2, the unloaded Fe-Arm is subjected to a passive evaluation experiment setup. A thin inelastic soft cord is attached to the end plate of the Fe-Arm and fixed to a point in space. Upon releasing the cord, the Fe-Arm exhibits an immediate tendency to restore its original vertical state. This behavior is attributed to the internal actuation force resulting from the pressure difference between the actuators' cavities and the reaction force arising from structural deformation. To capture and analyze the Fe-Arm's motion, an inertial measurement unit (MPU-6050) is mounted on the end plate. This allows for the recording of pitch angle and acceleration data during the motion of the Fe-Arm. By evaluating the extent of vibration and the settling time in the restoring process, valuable insights can be obtained regarding the impact of different designs on the foam-embedded system's performance.

To facilitate the comparison of different foam-embedded designs in the passive evaluation experiment, we propose four metrics to assess their performance: (a) a_{peak}: The peak acceleration experienced by the end plate of the Fe-Arm. (b) T_{stable}: The relative stability time is defined as the duration required for the Fe-Arm to reach the quasi-static state. It is determined by identifying the time instant when the third peak of the pitch angle is reached. (c) $T_{settling}$: The settling time is defined as the duration it takes for the acceleration of the Fe-Arm to reduce to a range between 0.85g and 1.05g, which corresponds to a 5% error relative to the steady-state acceleration. (d) Δ_{angle}: This metric quantifies the angular difference between the final state of the Fe-Arm and its initial vertical state after stabilization.

C. Configuration Iteration

We conducted experiments to achieve the foam-embedded design, focusing on three key aspects. Firstly, we compare two different materials, high-resilience foam and memory foam, with no foam to evaluate the impact of foam material on the arm's performance. Next, we explored the influence of foam density by testing three different density levels. Lastly, we investigated the effect of two geometrical parameters: the length of the gap between levels (L_{gap}) and the length of the initial compression (L_{ic}), as shown in Fig. 1(d). L_{gap} brings more flexibility for the foam between levels of the joints. With larger L_{ic}, the actuators can extend easier with less constraint from the foam due to the easy-to-compressed and hard-to-elongated characteristics of the foam. For each of these optimization aspects, we performed the passive evaluation experiment and utilized the metrics mentioned to evaluate and compare the performance of the optimized designs.

The passive evaluation experiment results are shown in Fig. 3. In the comparison experiment of different foam materials, memory foam stands out by manifesting a significant reduction in a_{peak} of 3.4g and $T_{settling}$ of 0.4s, compared to the other two designs. Although the T_{stable} of 0.8s is longer than that of the high-resilience foam (0.66s), the latter exhibits more oscillations in subsequent movements and a large Δ_{angle} of -9.9°. These observations underscore that memory foam is a suitable choice for mitigating oscillations and improving performance, a result attributed to its superior viscoelastic and low-resilience characteristics.

To investigate the impact of foam density, we conducted comparison tests using different densities of memory foam: 50D, 65D, and 90D. The results show that the 65D memory foam exhibits similar performance to the 50D memory foam in terms of T_{stable} of 0.81s and $T_{settling}$ of 0.4s. However, it significantly outperforms the 50D memory foam in a_{peak} with a value of 3g. On the other hand, the 90D memory foam demonstrates a large Δ_{angle} of -10.2°. Consequently, the 65D memory foam is considered to be the better choice in terms of foam density.

The geometrical design parameters were optimized using 65D memory foam. Comparative tests were conducted using

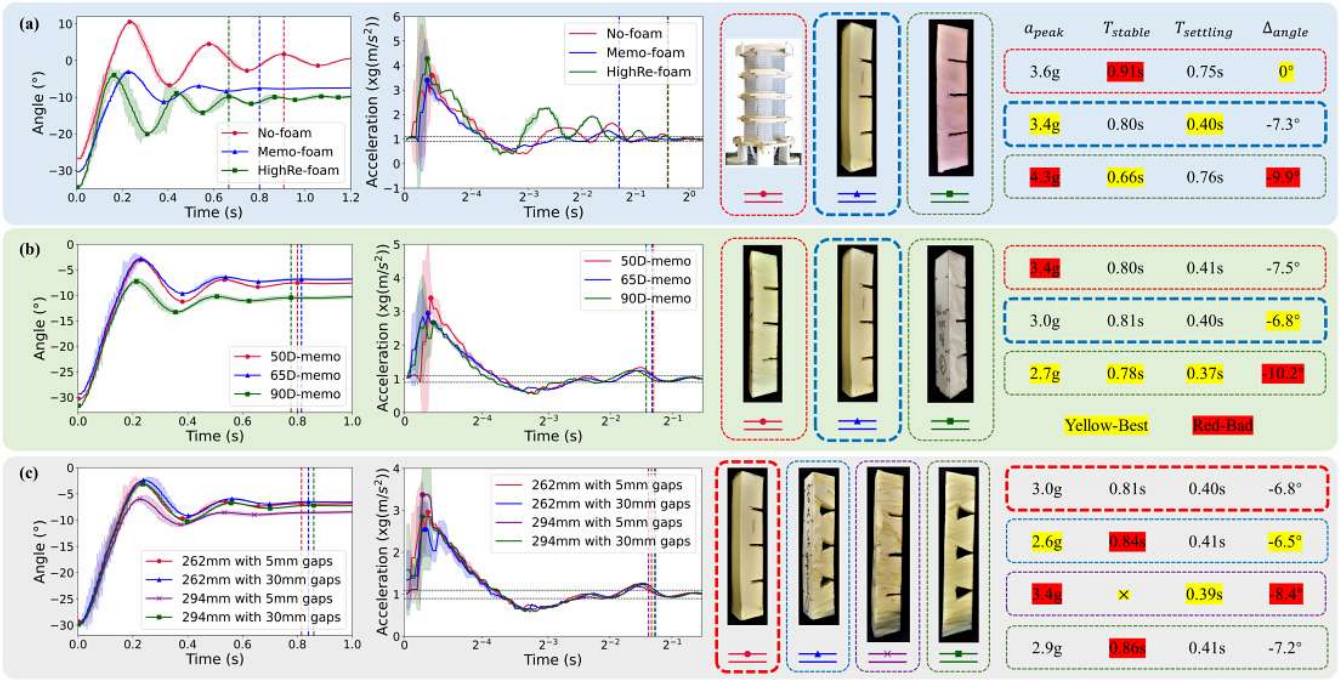

Fig. 3. Passive evaluation experiment results. From left to right are, respectively, angular and acceleration graphs, physical photos of the design used, and values of four metrics. a_{peak}: peak dots in the acceleration graphs; T_{stable}: dashed lines in the angle graphs; $T_{settling}$: dashed lines in the acceleration graphs; Δ_{angle}: values of the end of curves in the angle graphs. Distinct designs are represented by varying colors of curves and dashed edges. The chosen designs are accentuated with thickened dashed edges. (a) Material comparison. (b) Density comparison. (c) Geometrical parameters comparison.

262mm and 294mm values for L_i (equivalent to 28mm and 60mm L_{ic}), 5mm and 30mm values for L_{gap}. It was observed that the designs with 5mm gaps exhibited excellent performance in terms of T_{stable} and $T_{settling}$ compared to the 30mm gap designs. However, the 294mm design with 5mm gaps showed a relatively large Δ_{angle} of -8.4°, and the difference in a_{peak} between the 262mm design with 30mm and 5mm gaps was not substantial. Overall, the configuration with 262mm L_i and 5mm L_{gap} yielded the relatively best performance among the tested designs. Therefore, the 262mm L_i and 5mm L_{gap} 65D memory foam was chosen as the basis for further research, and the modeling of the Fe-Arm was implemented based on this configuration.

D. Sensing and Motion Control

The end position of the Fe-Arm is measured using the Orbbec Astra Mini monocular RGB depth camera, as shown in Fig. 4(a). This process involves identifying the blue sticker on the end plate and extracting the center point's coordinates from the point cloud data. The pneumatic actuation module consists of the micro-controller unit (MCU), solenoid valves, pressure sensors, and other parts, as shown in Fig. 4(b). The STM32F103C8T6 is used as the MCU to control the whole system. The air pressure sensors are connected in series with the output air circuit to measure the three actuation pressures of the Fe-Arm respectively.

Using pneumatic control without any feedback, the Fe-Arm is capable of executing simple movements within its workspace with manual control inputs. The trajectories of the Fe-Arm in the vertical, side, and forward three DOFs, along with the corresponding actuation pressure values, are depicted in Fig. 4(c-e), respectively. Specifically, the Fe-Arm can achieve a lateral 90° bend, a longitudinal contraction of 125mm, and an extension of 15mm relative to its initial length, as demonstrated in Fig. 4(d). The maximum horizontal radius of motion is 160mm, as shown in Fig. 4(c). These basic movements showcase the feasibility and mechanical properties of the Fe-Arm after embedding with foam.

III. Iterative Self-Improving Learning for End-to-End Inverse Kinematic Modeling

A. Modeling Method Architecture

Due to the foam-embedded structure of the Fe-Arm, the material property of memory foam has the capacity to store motion potential energy and subsequently release it slowly. As a result, the present state of the Fe-Arm is notably influenced by its preceding state during continuous movement. This dynamic gives rise to an intractable scenario where a specific set of pressure values within the actuation space may correspond to multiple distinct end positions in the task space, depending on the entire trajectory the arm traveled from.

To effectively capture and respond to the intricate relationship between the sequence of antecedent states and the current state of the Fe-Arm, we employ RNNs for data-driven end-to-end inverse kinematic modeling. RNNs, as a specialized form of neural network, excel in processing sequential data. Their outputs are determined by the inputs and the internally stored states derived from prior computations. This property allows RNNs to capture the Fe-Arm's states in previous time steps. Specifically, we utilize the LSTM model [28] within the RNN

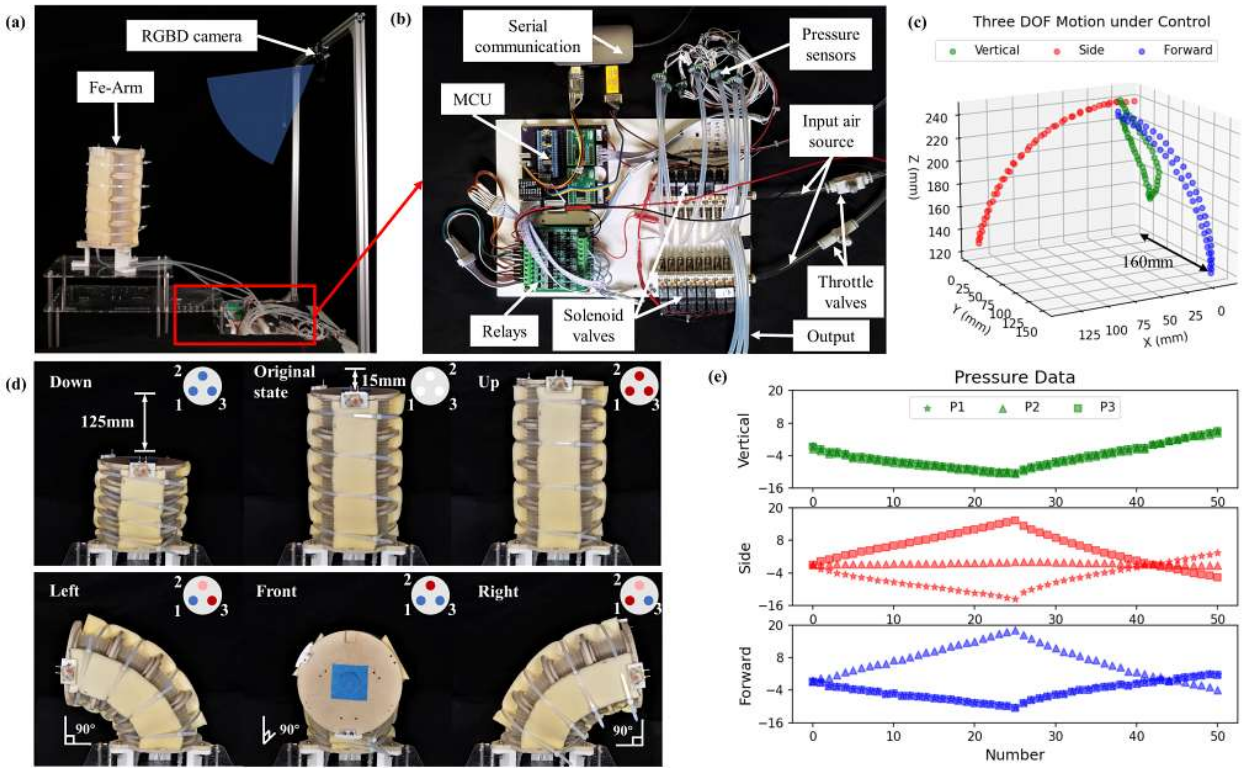

Fig. 4. (a) End position detection module. (b) Pressure measurement and control module. (c) Motion trajectories of three DOFs. (d) Mechanical performance demonstration of the Fe-Arm. Blue indicates deflate, red indicates inflate, and white indicates atmospheric pressure. Color shades correspond to bellows' internal pressure level. (e) Corresponding actuation pressure values of motion in three DOFs.

framework to address this particular challenge. The underlying principle is illustrated below, encompassing valuable insights from all preceding data points:

$$p(k) = f^{-1}(p(0), p(1), ..., p(k-1), t(k)), \tag{1}$$

where the input pressure values of the actuators at the moment k are represented by $p(k)$, denoting the actuation space; the corresponding target space end position of the Fe-Arm is denoted by $t(k)$.

When using traditional data-driven training methods, a substantial volume of high-quality motion data is necessary to achieve accurate modeling and prediction of the intended trajectory. However, the expenses associated with procuring the requisite training data result in a cumbersome sensing and controller preparation process. This situation fails to fully exploit the inherent ease of the learning approach in facilitating the simplified modeling of the Fe-Arm.

To address this, we propose an iterative self-improving learning (ISL) strategy designed to accomplish modeling for a specific target trajectory using a limited dataset. The agent starts with a limited amount of labeled data. Then the agent uses the available labeled data to make predictions, which are then applied to the Fe-Arm. This results in obtaining real actuation pressure and end position data. However, due to the scarcity of high-quality data, the actual motion trajectories exhibit significant deviations from the target trajectories. These low-quality real motion data are then reintroduced into the training set for continuous iteration. Through iterative training on this combined set of labeled and low-quality data, the proposed learning strategy effectively generates more training samples and improves the model's performance with minimal human intervention. The overall modeling method procedure is illustrated in Fig. 5, with the red section depicting the process of the ISL.

B. Data Acquisition

Due to the symmetry of the Fe-Arm structure, our investigation is focused on the forward 120° workspace, as shown by the light green region in Fig. 6(a), for the sake of simplicity. The modeling method can be extended to the entire workspace.

As an initial model needs to be obtained before the self-improving iterations can be performed, we also collect a simple initial training set. The initial training set contains four sets of the simplest and easiest to control trajectories, which are the forward, both sides of the 60° vertical plane, and the vertical direction. Each set of data is a downward motion from the original vertical state and then returns upward back, as shown in Fig. 6(a). The Fe-Arm was first fixed at the original vertical position using external support structures to ensure consistency for each experiment. Then remove the supports and start actuating. Each completed actuation immediately reads the three pressure values at that time. After waiting for several seconds, the Fe-Arm reaches quasi-static, and the camera takes a photo and measures the coordinates of the end position at this point. The complete data set contains the three actuation pressures and the 3D position coordinates of all data points. All data acquisition and testing are performed according to this process.

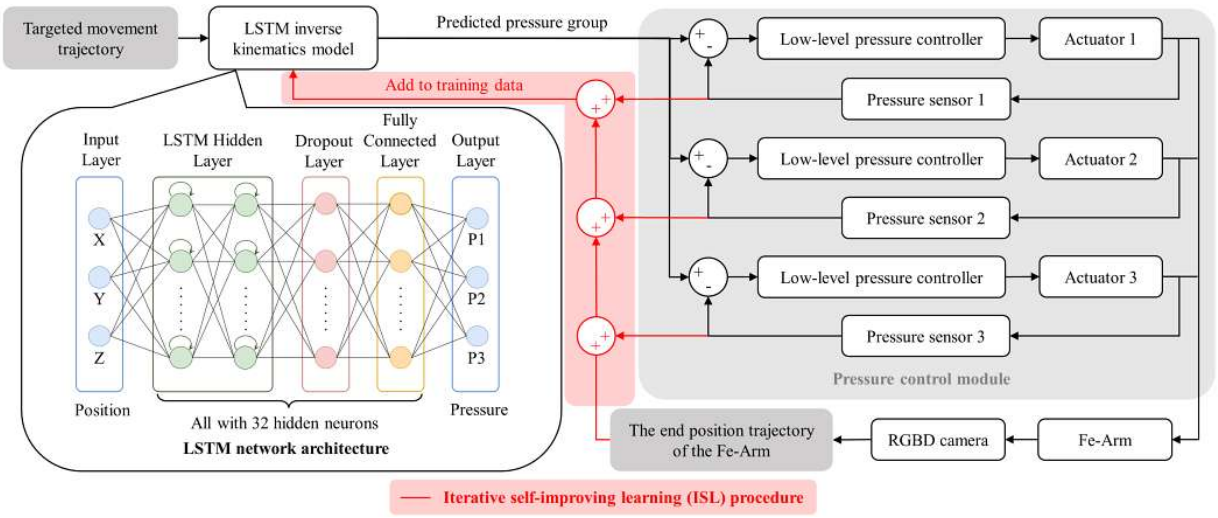

Fig. 5. Schematic diagram of the LSTM-based iterative self-improving learning method (ISL) for end-to-end inverse kinematic modeling.

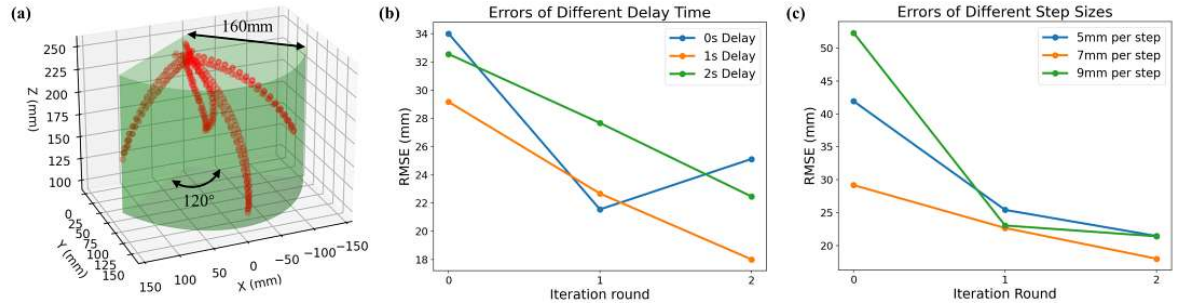

Fig. 6. (a) Initial training set and focused workspace. (b) The effects of different delay times on modeling. (c) The effects of different step sizes on modeling.

C. Neural Network Design and Training

We use PyTorch for building models, training, and inference. The specific LSTM-based model architecture we use is shown in Fig.5. The network commences with a sequential input layer, incorporating three dimensions (3D) of end position coordinates, relative to the coordinate system anchored at the base of the Fe-Arm. It is followed by two LSTM hidden layers, each comprising 32 hidden neurons. To prevent overfitting and to make the prediction and modeling more robust to noise, a dropout layer is added after the LSTM layer, with a dropout rate of 0.2. This is followed by a fully connected linear mapping layer of the same size for mapping the position to the pressure. Finally, the output layer produces the three internal actuation pressure values. The training process utilizes the adaptive moment estimation (Adam) algorithm to expedite convergence and efficacy. The mean squared error loss function (RMSE) is used as the loss function. The number of training epochs is 200.

D. Parameters Optimization

Two critical parameters that influence the inverse kinematics modeling during the control process are the time to wait to reach quasi-stasis after each step (T_{delay}) and the distance between each small step (L_{step}). Considering the Fe-Arm need to ensure the quasi-static state during inverse kinematics modeling, the memory foam's slow rebound property requires a delay time after each actuation. A brief delay might prevent the Fe-Arm from reaching quasi-static. On the other hand, a prolonged delay could disrupt motion continuity. Simultaneously, a larger step size results in a smaller sampling frequency. Conversely, a smaller step size can introduce higher randomness fluctuations due to systematic errors. Therefore, finding the right balance between these two parameters is crucial to achieving accurate and stable inverse kinematics modeling while ensuring smooth and continuous robot motion.

We conducted two rounds of iterations using the same target trajectory (lower quadrilateral, as shown in Fig. 7(a)), comparing the effects of different delay times (0s, 1s, 2s) and step sizes (5mm, 7mm, 9mm) on modeling accuracy. The results are depicted in Fig. 6(b)(c). Notably, optimal modeling performance was consistently achieved with the middle values of T_{delay} and L_{step}, specifically 1s delay and 7mm per step. These values yielded the least error across multiple rounds. In round 2, errors reached a minimum of 18.00mm and 21.45mm, respectively. The corresponding percentage errors relative to the maximum horizontal radius of motion are 11.25% and 13.4%. Importantly, both parameter values demonstrated significant improvement trends during iterations. As a result, we have chosen these two values as the control parameters for subsequent modeling tasks.

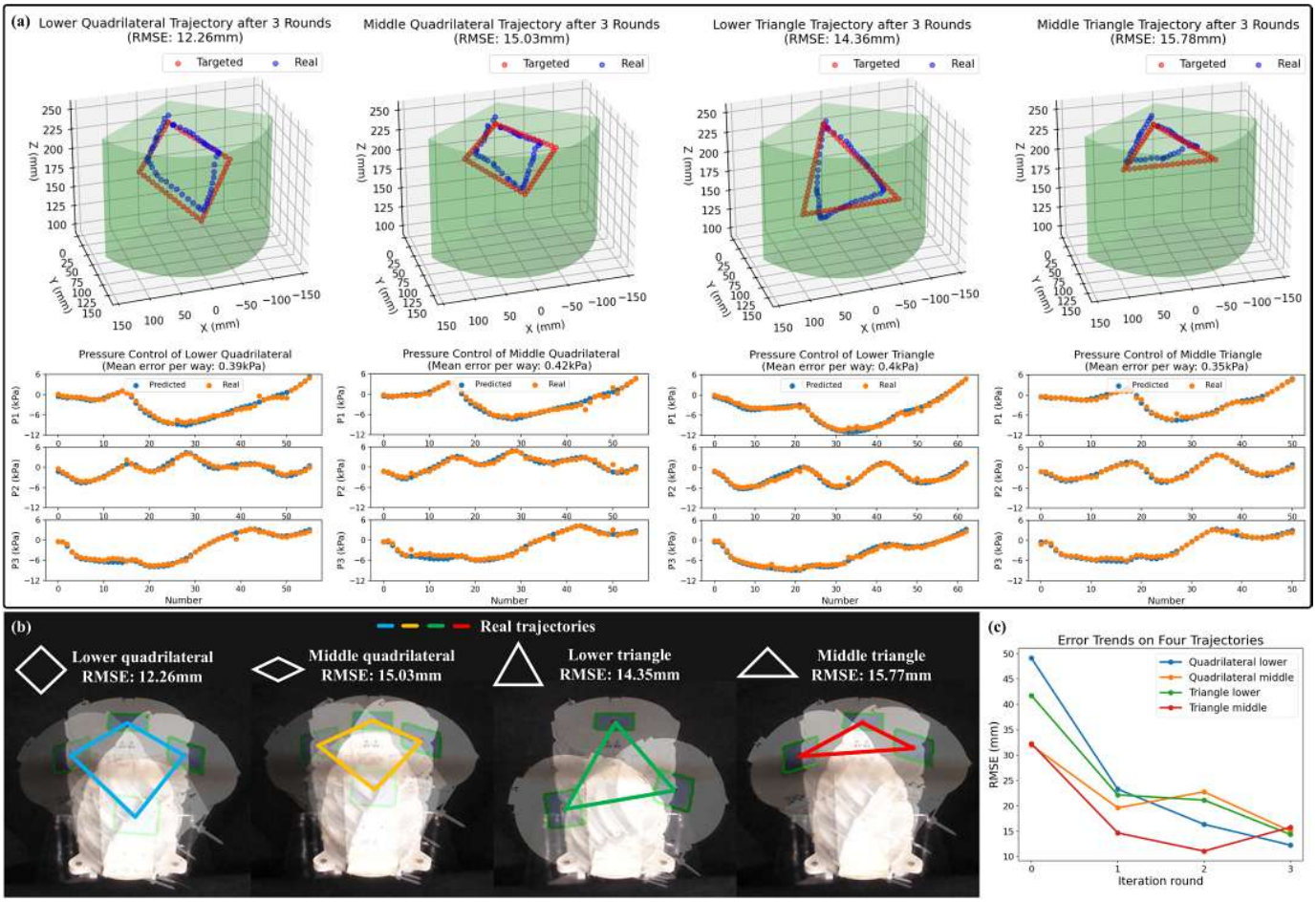

Fig. 7. (a) Modeling results of four trajectories after three round iterations. The above row shows the 3D position comparison between the target trajectories and the real trajectories. The row below shows the comparison of the predicted pressure values and the actual feedback control values for the corresponding trajectories. (b) Photos of parts of motion trajectories shoot by RGBD camera. (c) The RMSEs of the real trajectories compared to the target trajectories.

TABLE II
THE PERCENTAGE ERRORS OF FOUR TRAJECTORIES RELATIVE TO THE MAXIMUM HORIZONTAL RADIUS OF MOTION

Trajectories	Round 0	Round 1	Round 2	Round 3
Lower Quadrilateral	30.69%	14.55%	10.22%	**7.67**%
Middle Quadrilateral	19.96%	12.25%	14.22%	**9.40**%
Lower Triangle	26.08%	13.85%	13.21%	**8.97**%
Middle Triangle	20.15%	9.16%	**6.92**%	9.86%

E. Modeling Results

We designed four different movement trajectories, consisting of two different sizes of quadrilaterals and triangles, as shown in Fig. 7. We employed the ISL strategy outlined above to train a unified model using data collected from all four trajectories, in both clockwise and counterclockwise directions. Fig. 7(a)(b) illustrate the trajectory outcomes in 3D space and through real images, after three rounds of self-improving iterations, respectively. The RMSEs of the real trajectories controlled with predicted pressure compared to the target trajectories are presented in Fig. 7(c). Additionally, the corresponding percentage errors relative to the maximum horizontal radius of motion are summarized in TABLE II. Across three round iterations, the RMSEs for all four motion trajectories remained below 16mm, with relative errors consistently within 10%. Notably, the smallest modeling error after three iterations was observed in the lower quadrilateral, measuring 12.26mm and 7.67%. The actual control mean absolute deviation (MAD) of the pressure feedback control process for the target actuation pressure per way is 0.39 kPa.

The application of the ISL for end-to-end inverse kinematics modeling of the Fe-Arm has demonstrated both practicality and accuracy. Since system error is introduced due to the incompleteness of feedback pressure control accuracy, the true accuracy of this modeling technique is anticipated to surpass the reported outcomes. Furthermore, the proposed learning strategy enhances model prediction accuracy as iterations progress. Particularly noteworthy is the observed reduction of the middle triangle's error to 11.08mm in the second iteration, which implies that modeling errors tend to stabilize and converge with an increase in iterations due to control and system factors. In summary, the collective findings illustrate that this ISL modeling approach attains superior accuracy even with a limited number of iterations and a constrained dataset of high quality. This performance underscores the methodology's efficacy and practical applicability.

IV. Conclusion

This paper has effectively tackled critical challenges within soft robotic arms, focusing on the issues of oscillation and instability during control. Through the utilization of memory foam's unique viscoelastic and low-resilience characteristics, we have successfully engineered a Fe-Joint design that suppresses oscillations during motion. This innovation has been incorporated into the Fe-Arm, a continuum soft robotic arm, with an iterative optimization process refining design configurations. The resultant mechanical performance of the Fe-Arm showcases exceptional control potential across stability and an expansive workspace, all while retaining its inherent flexibility and compliance. After being subjected to substantial external forces resulting in a 30° deflection, the Fe-Arm achieves a settling state in a mere 0.4 seconds, swiftly transitioning to a quasi-static state in 0.8 seconds, capping the maximum acceleration at less than 3g, and yielding a final error of 6.8° from the vertical state. Notably, the Fe-Arm excels in performing a lateral 90° bend and 160mm maximum horizontal radius of motion, contracting longitudinally by 125mm and extending by 15mm relative to its initial length.

Furthermore, we introduced an LSTM-based iterative self-improving end-to-end inverse kinematics modeling method, specifically tailored to the Fe-Arm's mechanical intricacies. Through the optimization of control parameters, our methodology achieved trajectory modeling errors consistently less than 16mm and a mere 10% in relation to the workspace radius. The best modeling result, after three rounds of iterations, reached an error of 12.26mm and 7.67%. These results were achieved while working with restricted datasets, iteration cycles, and limited human intervention. Furthermore, our proposed learning strategy progressively enhanced model prediction accuracy throughout the iterative process, exemplifying its efficacy in ensuring precise trajectory tracking under open-loop control paradigms.

For future research, we will conduct several promising directions. Enhancing controller precision and integrating advanced sensing technologies to encompass angular information and expand the range of motion regions within the inverse kinematics framework.

References

[1] D. Rus and M. T. Tolley, "Design, fabrication and control of soft robots," *Nature*, vol. 521, no. 7553, pp. 467–475, 2015.

[2] C. Laschi, B. Mazzolai, and M. Cianchetti, "Soft robotics: Technologies and systems pushing the boundaries of robot abilities," *Science Robotics*, vol. 1, no. 1, p. eaah3690, 2016.

[3] A. D. Marchese and D. Rus, "Design, kinematics, and control of a soft spatial fluidic elastomer manipulator," *The International Journal of Robotics Research*, vol. 35, no. 7, pp. 840–869, 2016.

[4] T.-D. Nguyen and J. Burgner-Kahrs, "A tendon-driven continuum robot with extensible sections," in *2015 IEEE/RSJ International Conference on Intelligent Robots and Systems (IROS)*. IEEE, 2015, pp. 2130–2135.

[5] C. Laschi, M. Cianchetti, B. Mazzolai, L. Margheri, M. Follador, and P. Dario, "Soft robot arm inspired by the octopus," *Advanced robotics*, vol. 26, no. 7, pp. 709–727, 2012.

[6] P. Qi, C. Qiu, H. Liu, J. S. Dai, L. D. Seneviratne, and K. Althoefer, "A novel continuum manipulator design using serially connected double-layer planar springs," *IEEE/ASME Transactions on Mechatronics*, vol. 21, no. 3, pp. 1281–1292, 2015.

[7] M. Rolf and J. J. Steil, "Efficient exploratory learning of inverse kinematics on a bionic elephant trunk," *IEEE transactions on neural networks and learning systems*, vol. 25, no. 6, pp. 1147–1160, 2013.

[8] V. Falkenhahn, A. Hildebrandt, R. Neumann, and O. Sawodny, "Dynamic control of the bionic handling assistant," *IEEE/ASME Transactions on Mechatronics*, vol. 22, no. 1, pp. 6–17, 2016.

[9] C. Yang, S. Geng, I. Walker, D. T. Branson, J. Liu, J. S. Dai, and R. Kang, "Geometric constraint-based modeling and analysis of a novel continuum robot with shape memory alloy initiated variable stiffness," *The International Journal of Robotics Research*, vol. 39, no. 14, pp. 1620–1634, 2020.

[10] Y. Li, T. Ren, Y. Chen, and M. Z. Chen, "A variable stiffness soft continuum robot based on pre-charged air, particle jamming, and origami," in *2020 IEEE International Conference on Robotics and Automation (ICRA)*. IEEE, 2020, pp. 5869–5875.

[11] J. Liu, X. Wang, S. Liu, J. Yi, X. Wang, and Z. Wang, "Vertebraic soft robotic joint design with twisting and antagonism," *IEEE Robotics and Automation Letters*, vol. 7, no. 2, pp. 658–665, 2021.

[12] B. C. Mac Murray, X. An, S. S. Robinson, I. M. van Meerbeek, K. W. O'Brien, H. Zhao, and R. F. Shepherd, "Poroelastic foams for simple fabrication of complex soft robots," *Advanced Materials*, vol. 27, no. 41, pp. 6334–6340, 2015.

[13] S. Li, S. A. Awale, K. E. Bacher, T. J. Buchner, C. Della Santina, R. J. Wood, and D. Rus, "Scaling up soft robotics: A meter-scale, modular, and reconfigurable soft robotic system," *Soft Robotics*, vol. 9, no. 2, pp. 324–336, 2022.

[14] L. Somm, D. Hahn, N. Kumar, and S. Coros, "Expanding foam as the material for fabrication, prototyping and experimental assessment of low-cost soft robots with embedded sensing," *IEEE Robotics and Automation Letters*, vol. 4, no. 2, pp. 761–768, 2019.

[15] M. A. Robertson and J. Paik, "New soft robots really suck: Vacuum-powered systems empower diverse capabilities," *Science Robotics*, vol. 2, no. 9, p. eaan6357, 2017.

[16] A. Sfaoui, "On the viscoelasticity of the polyurethane foam," *The Journal of the Acoustical Society of America*, vol. 97, no. 2, pp. 1046–1052, 1995.

[17] M. A. Garrido, R. Font, and J. A. Conesa, "Kinetic study and thermal decomposition behavior of viscoelastic memory foam," *Energy Conversion and Management*, vol. 119, pp. 327–337, 2016.

[18] R. J. Webster III and B. A. Jones, "Design and kinematic modeling of constant curvature continuum robots: A review," *The International Journal of Robotics Research*, vol. 29, no. 13, pp. 1661–1683, 2010.

[19] K. Chin, T. Hellebrekers, and C. Majidi, "Machine learning for soft robotic sensing and control," *Advanced Intelligent Systems*, vol. 2, no. 6, p. 1900171, 2020.

[20] X. Wang, Y. Li, and K.-W. Kwok, "A survey for machine learning-based control of continuum robots," *Frontiers in Robotics and AI*, p. 280, 2021.

[21] G. Fang, Y. Tian, Z.-X. Yang, J. M. Geraedts, and C. C. Wang, "Efficient jacobian-based inverse kinematics with sim-to-real transfer of soft robots by learning," *IEEE/ASME Transactions on Mechatronics*, vol. 27, no. 6, pp. 5296–5306, 2022.

[22] R. B. Scharff, G. Fang, Y. Tian, J. Wu, J. M. Geraedts, and C. C. Wang, "Sensing and reconstruction of 3-d deformation on pneumatic soft robots," *IEEE/ASME Transactions on Mechatronics*, vol. 26, no. 4, pp. 1877–1885, 2021.

[23] L. Wang, J. Lam, X. Chen, J. Li, R. Zhang, Y. Su, and Z. Wang, "Soft robot proprioception using unified soft body encoding and recurrent neural network," *Soft Robotics*, 2023.

[24] G. Kahn, P. Abbeel, and S. Levine, "Badgr: An autonomous self-supervised learning-based navigation system," *IEEE Robotics and Automation Letters*, vol. 6, no. 2, pp. 1312–1319, 2021.

[25] L. Berscheid, T. Rühr, and T. Kröger, "Improving data efficiency of self-supervised learning for robotic grasping," in *2019 International Conference on Robotics and Automation (ICRA)*. IEEE, 2019, pp. 2125–2131.

[26] C. Rosenberg, M. Hebert, and H. Schneiderman, "Semi-supervised self-training of object detection models," 2005.

[27] Q. Xie, M.-T. Luong, E. Hovy, and Q. V. Le, "Self-training with noisy student improves imagenet classification," in *Proceedings of the IEEE/CVF conference on computer vision and pattern recognition*, 2020, pp. 10 687–10 698.

[28] S. Hochreiter and J. Schmidhuber, "Long short-term memory," *Neural computation*, vol. 9, no. 8, pp. 1735–1780, 1997.